CrossMark

Controllable synthesis of MoO$_3$-deposited TiO$_2$ nanotubes with enhanced lithium-ion intercalation performance

Dongsheng Guan, Jianyang Li, Xianfeng Gao, Chris Yuan*

The Department of Mechanical Engineering, University of Wisconsin Milwaukee, Milwaukee, WI 53211, USA

HIGHLIGHTS

- MoO$_3$-coated TiO$_2$ nanotube arrays were firstly fabricated and reported as LIB anode.
- The MoO$_3$-coated TiO$_2$ nanotube anode increased the areal capacity significantly.
- The coated TiO$_2$ nanotube anode showed improved rate capability and cycleability.
- Increasing dimensions of MoO$_3$-coated TiO$_2$ nanotubes yields superior areal capacity.
- The deposition cycle was optimized to gain the best performance of MoO$_3$/TiO$_2$ anode.

ARTICLE INFO

ABSTRACT

Well-organized TiO$_2$ nanotube arrays are synthesized by anodic oxidation and then modified with MoO$_3$ via facile electrodeposition for their improved Li-ion intercalation property. All the bare and MoO$_3$-deposited TiO$_2$ nanotubes are cycled at a current of 50 or 200 μA cm^{-2}. The deposited nanotubes surprisingly deliver twice or even triple areal capacity of the bare ones, as well as better rate capability. For example, the bare nanotubes exhibit an initial capacity of 81.2 μAh cm^{-2} and a final capacity of 59.6 μAh cm^{-2} over 48 electrochemical cycles, while the ones coated by MoO$_3$ using only one deposition cycle displays a nearly doubled initial capacity of 154.9 μAh cm^{-2} and a final capacity of 116.6 μAh cm^{-2}. More deposition cycles yield TiO$_2$ nanotubes with higher capacities up to 204.7 μAh cm^{-2}. Such improvement could be further optimized by tuning the dimensions of TiO$_2$ nanotubes. An eight-fold increase in the capacity of MoO$_3$/TiO$_2$ nanotube composite anode is achieved easily with larger nanotubes for MoO$_3$ coating. This is attributed to the combination of MoO$_3$ with a high specific capacity and TiO$_2$ nanotubes with large surface area allowing efficient MoO$_3$ deposition and ionic transport inside the anode.

1. Introduction

Currently, soaring development in electronic devices and electric vehicles urgently demands mobile power sources with high energy capacity, power density and durability, and good safety in restricted volume and weight. Rechargeable lithium-ion batteries (LIBs) have become an excellent candidate because of their high energy density, light weight, no memory effects, low self discharge and long lifespan [1,2]. Graphite is the most commonly-used anode material in commercial LIBs at present, but its drawbacks (easy formation of hazardous lithium dendrites) hinder innovation of compact LIBs with higher energy density and better cell safety [3]. As a result, novel anode materials have been developed to replace it, such as Si [4], Sn [5], Al [6], alloys [7], MoO$_3$ [8], Co$_3$O$_4$ [9], SnO$_2$ [10], WO$_3$ [11], SiO$_2$ [12], Li$_4$Ti$_5$O$_{12}$ [13] and TiO$_2$ [14]. Among them TiO$_2$ is a promising alternative to the graphite because of its high operation voltage (1.75 V versus Li/Li$^+$), high safety, good cycleability, low self-discharge rates and small volume change (<3%) during cycle use in LIBs [15]. It is also attractive for abundant resource, low cost, chemical stability and environmental friendliness. Nanostructured TiO$_2$, such as TiO$_2$ nanoparticles, nanowires, nanorods and nanotubes boosts the application of TiO$_2$ in LIBs, due to their small size but large surface favorable for more Li-ion insertion and faster diffusion [16].

Self-organized TiO$_2$ nanotube arrays can be easily synthesized by anodic oxidation of Ti in fluoride-containing electrolytes [17]. A well-ordered structure and double-sided tube walls, together with metal substrate directly serving as a current collector, intrinsically endow them to be an excellent anode material for LIBs [18–20]. However, the poor Li-ion intercalation nature of TiO$_2$ restricts their battery applications. For example, anatase TiO$_2$ can only possess a

* Corresponding author. Tel.: +1 414 229 5639; fax: +1 414 229 6958.
  E-mail address: cyuan@uwm.edu (C. Yuan).

small theoretical capacity ($\sim$168 mAh g^{-1}), even lower than half that of graphite ($\sim$372 mAh g^{-1}). Therefore, TiO$_2$ nanotubes need to be improved urgently in order to meet the demands for LIBs with high energy density and power density used as power sources in EVs and HEVs. Three primary methods have been proposed to deal with this problem. The first one is to dope TiO$_2$ nanotubes with metal or nonmetal elements, such as Sn [21], C [22] and N [23]. The second one is to coat them with conductive reagents, such as Sn [24], Ni [25] and Ag [26]. The final one is to modify them by other anode materials with larger capacities to yield hybrid or composite structures. For example, TiO$_2$ nanotube composites with SnO$_2$ [27], NiO [28], Co$_3$O$_4$ [29,30], Nb$_2$O$_5$ [31], Fe$_2$O$_3$ [32] and Cu$_6$Sn$_5$ [33] have been seen in literature.

Alpha-phase molybdenum trioxide (α-MoO$_3$) is a well-known anode material for LIBs, with an extraordinarily high theoretical capacity (1111 mAh g^{-1}). It has a stable layered orthorhombic structure that is able to temporarily accommodate and release Li$^+$ ions. However, its composite with anodic TiO$_2$ nanotubes for LIB applications surprisingly has not been reported hitherto. Consequently, we propose synthesis of a heterogenous MoO$_3$/TiO$_2$ nanotube structure by cyclic electrodeposition strategy on the basis of these reasons: (i) α-MoO$_3$ on TiO$_2$ nanotubes could be inserted by as many Li$^+$ ions as needed for significant enhancement of TiO$_2$ anode; (ii) the high-aspect-ratio and top-open TiO$_2$ nanotubes have large surface area for MoO$_3$ deposition and rapid Li-ion transfer; (iii) TiO$_2$ has negligible lattice change during cycling, but MoO$_3$ shows volume changes up to 200% [34], and thus TiO$_2$ nanotubes can act as a stable framework to sustain or restrict MoO$_3$ particles with varied shapes, (iv) TiO$_2$ nanotubes not only transfer electrons for MoO$_3$, but also contribute to the overall capacity of composite anode, (v) the electrodeposition method is a facile, controllable and applicable one for efficient formation of MoO$_3$; (vi) a self-standing and binder-free anode could be easily achieved for LIBs to reduce production costs.

In the present work, well-aligned TiO$_2$ nanotube arrays were synthesized by potentiostatic anodization. Heat treatment converted as-prepared nanotubes into anatase for electrodeposition of MoO$_3$. The amount of MoO$_3$ was optimized by varying the number of deposition cycles in order to obtain the nanotube composite anodes with the best Li-ion insertion performance. In addition, the influencing mechanism of MoO$_3$ coating on the Li-ion intercalation behaviors of TiO$_2$ anode was also explored. Moreover, the impact of dimensions of TiO$_2$ nanotubes on the morphology and charge–discharge property of these composite anodes was investigated.

2. Experimental

Titanium foils (99.5 wt%, 250 μm thick) were purchased from Alfa Aesar, USA. Prior to electrochemical treatment, the Ti foils were degreased and rinsed by sonicating in ethanol and deionized water, and then covered by Scotch tape at their back. A two-electrode cell composed of a Ti foil as working electrode and a Pt foil as counter electrode was assembled for anodization. Small TiO$_2$ nanotubes (designated as B-ST) were synthesized in ethylene glycol (EG, Alfa Aesar) electrolytes containing 0.3 wt% NH$_4$F (MP Biomedicals, USA) and 10 vol% H$_2$O at 60 V for 30 min, while large nanotubes (designated as B-LT) were produced in EG electrolytes with 0.3 wt% NH$_4$F and 5 vol% H$_2$O at 70 V for 40 min. After anodization was completed, the sample was immediately rinsed with deionized water, dried and annealed at 450 $^\circ$C for 1 h in air, to obtain crystalline TiO$_2$ nanotubes. Later, electrochemical deposition of MoO$_3$ onto these nanotubes was carried out using a VersaSTAT 3F potentiostat/galvanostat with FRA (Princeton Applied Research, USA) with a three-electrode setup composed of anodized Ti as the working electrode, a Pt foil as the counter electrode and an Ag/AgCl

reference electrode. The deposition process was performed in 0.05 M (NH$_4$)$_6$Mo$_7$O$_{24}$ (Alfa Aesar) aqueous solution by cycling from 0 to -0.7 V with a step rate of 20 mV s^{-1} for 1 to 6 cycles. Deposited small and large TiO$_2$ nanotubes are designated as MO-ST and MO-LT plus electrodeposition cycle number. All the bare and deposited TiO$_2$ samples were then annealed in air at 450 $^\circ$C for 1 h for battery testing. We estimated the mass of anatase TiO$_2$ nanotubes on Ti substrates through their amorphous phase, since their gravimetric change during crystallization is found to be negligible. Details are like this: Firstly, drying as-prepared TiO$_2$ nanotubes on Ti at 120 $^\circ$C for 1 h; Secondly, weighing the sample using a Sartorius Analytical Balance (CPA225D, with readability of 10 μg) before and after removing the amorphous nanotubes from Ti in 30 wt% H$_2$O$_2$ solution (Sigma–Aldrich). Likewise, we measured the mass of MoO$_3$ on TiO$_2$ nanotube films by weighing a sample before and after electrodeposition of MoO$_3$ and heat treatment at 450 $^\circ$C for 1 h. The total mass per square centimeter of B-ST, 1MO-ST, 2MO-ST, 4MO-ST, 6MO-ST and weight ratios of MoO$_3$ are approximately 0.62 mg (0%), 0.69 mg (9.82%), 0.71 mg (12.98%), 0.74 mg (15.93%) and 0.76 mg (18.04%), respectively. 4MO-LT ($\sim$2.60 mg, 15.3 wt% MoO$_3$) also shows more mass than B-LT ($\sim$2.20 mg).

A Hitachi S-4800 scanning electron microscope (SEM) was used to observe the morphology of bare and MoO$_3$-deposited TiO$_2$ nanotubes. The crystallographic structure of nanotubes was determined by X-ray diffraction (XRD) using a Scintag XDS 2000 X-Ray diffractometer with Cu K$_\alpha$ radiation at a scan rate of 2° min^{-1}. Chemical composition on the surface of TiO$_2$ nanotube arrays was characterized by an energy dispersive X-ray spectroscope (EDX) with an XFlash detector (Bruker AXS) on SEM, and an X-ray photoelectron spectroscope (XPS) on Hewlett–Packard 5950A spectrometer using a monochromatized Al K$_\alpha$ X-ray radiation source. All XPS spectra were calibrated by the binding energy of C1s peak at 284.8 eV.

CR2032 coin cells were then assembled to investigate electrochemical behaviors of bare and MoO$_3$-deposited TiO$_2$ nanotubes acting as the working electrode. A lithium disc served as the counter and reference electrode, which was separated from the nanotubes by a Celgard 20-μm-thick monolayer polyethylene membrane. Electrolytes were 1 M lithium hexafluorophosphate (LiPF$_6$) dissolved in a mixed solvent of ethylene carbonate and diethylene carbonate in 1:1 volume ratio (Novolyte Technologies, Inc). All the coin cells were assembled in an Ar-filled glove box with oxygen and moisture levels lower than 1 ppm. The galvanostatic charge–discharge cycling was carried out on LANHE automatic battery testers at a small current (10 or 40 μA cm^{-2}) for the first two cycles, and a large current (50–1000 μA cm^{-2}) for rest cycles. AC impedance measurements were also conducted on these cells at a test potential of $\sim$1.7 V (versus Li/Li$^+$) from 100 kHz to 0.1 Hz with a perturbation of 5 mV applied.

3. Results and discussion

Fig. 1 shows SEM images of TiO$_2$ nanotube arrays formed by anodizing Ti in EG + 0.3 wt% NH$_4$F + 10 vol% H$_2$O electrolyte at 60 V for 30 min, with and without subsequent MoO$_3$ deposit. The top-view SEM image in Fig. 1(a) shows a porous anodic TiO$_2$ film containing numerous pores with a diameter up to 65 nm. Under this porous surface are vertically-aligned hollow TiO$_2$ nanotubes with a length of $\sim$1.6 μm (B-ST, Fig. S1a). The nanotubes are connected by bamboo ridges (or rings) on their outer walls grown under constant-voltage anodization conditions [17]. Fig. 1(b) gives SEM image of TiO$_2$ nanotubes modified by MoO$_3$ via one deposition cycle (1MO-ST). Considerable particles are precipitated on the top of nanotube arrays, yielding fewer pores with a smaller size of $\sim$40 nm. They are believed to be molybdenum oxides according to previous reports [35,36]. These particles have edges and corners,
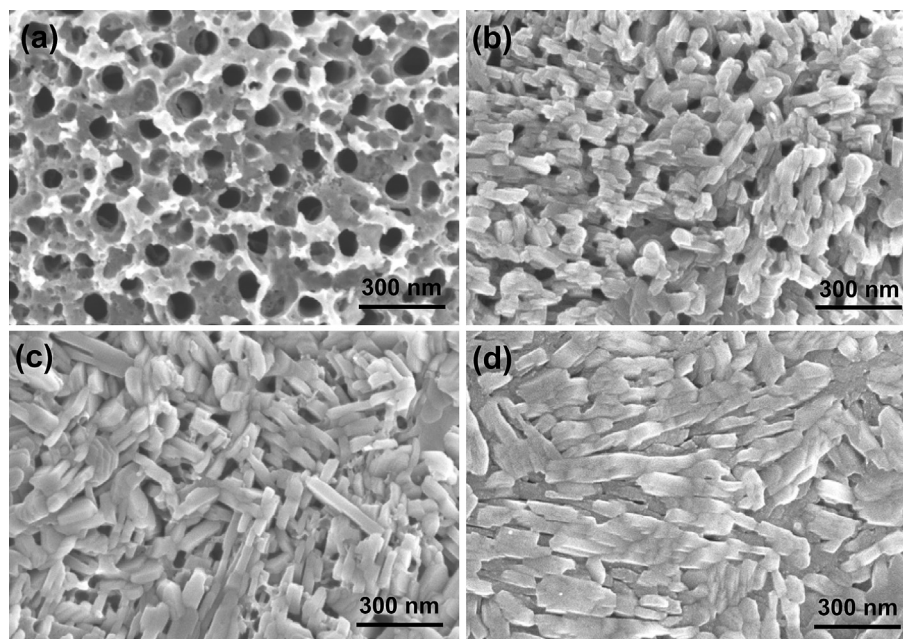
Fig. 1. SEM images of (a) B-ST, (b) 1MO-ST, (c) 2MO-ST and (d) 4MO-ST films synthesized by anodic oxidation of Ti in EG + 0.3 wt% NH_4F + 10 vol% H_2O at 60 V for 30 min and subsequent electrodeposition of MoO_3 via 0, 1, 2 and 4 cycles, respectively.

with a length up to 100 nm, and aggregate to cover the nanotube layer below. More molybdenum oxides are produced on the surface as the deposition cycle increases. Fig. 1(c) displays the morphology of TiO_2 nanotubes modified with two MoO_3 deposition cycles (2MO-ST), in which much fewer pores survive within the oxide film. It can be seen that more precipitates are produced on TiO_2 nanotubes, further aggregating to yield a loose film with low porosity. After four cycles of MoO_3 deposition, TiO_2 nanotubes are completely covered by large quantities of molybdenum oxides (4MO-ST, Fig. 1(d)). They are randomly dispersed, in the form of long particles with a length up to 370 nm and a width up to 130 nm. It should also be noted that the deposition of MoO_3 indeed reaches tube bottoms by the virtue of EDS examination on the top and bottom areas of 4MO-ST. Moreover, six MoO_3 deposition cycles on TiO_2 nanotubes result in a much denser and thicker MoO_3 layer composed of larger particles (6MO-ST, Fig. S1b). In conclusion, TiO_2 nanotube arrays have been successfully deposited by molybdenum oxides using the facile electrodeposition method, and the amount of precipitates can be readily adjusted by varying the deposition cycles. MoO_3 with a high specific capacity is likely to play an important role in the Li-ion intercalation process of deposited TiO_2 nanotubes in LIBs, and the morphology and performance of such composite anodes can be conveniently optimized through MoO_3 coating.

In order to prove the formation of molybdenum oxides on anodic TiO_2 nanotubes, both EDS and XPS techniques are employed to analyze the elemental composition and chemical states. Fig. 2(a) shows the EDS spectrum of 4MO-ST in which a strong peak at ~2.3 keV reveals the presence of molybdenum. Likewise, Ti and O elements are also detected from the sample. Al peak is generated from the aluminum holder used for placing the sample during EDS testing. In addition, the presence of molybdenum on deposited TiO_2 nanotubes is again confirmed by XPS analysis (Fig. 2(b)). It is demonstrated that Mo exist in the form of MoO_3 on nanotubes, because its two characteristic peaks of Mo3d5/2 at 233.0 eV and Mo3d3/2 at 236.1 eV ($\Delta E = 3.1$ eV) are observed, in agreement with the binding energy of Mo^{6+} ions in MoO_3 from Refs. [35,36]. Titanium peaks can be vividly found in the XPS pattern of B-ST, but

weaken greatly in that of 1MO-ST, and totally disappear for 4MO-ST (Fig. 2(c)), suggesting that the MoO_3 layer grown atop TO_2 nanotubes thickens along with more electrodeposition cycles. This is in accordance with the findings by SEM above. Fig. 2(d) gives O1s XPS peaks taken from the three samples. The peak at 530.3 eV is indexed to the Ti–O bond of TiO_2 in B-ST, while those at 531.1 eV correspond well to the Mo–O bond of MoO_3 in 1MO-ST and 4MO-ST. As a result, these characterization results indicate that the MoO_3-deposited TiO_2 nanotube arrays are achieved by controllable electrodeposition of MoO_3 on porous TiO_2 films.

Crystalline MoO_3 have various structures, among which α phase is well-known for its stable layer structure to accommodate many Li^+ ions and thus widely applied as an anode and cathode material in LIBs [34]. Fig. 3(a) illustrates the XRD patterns of B-ST and 4MO-ST. Typical diffraction peaks of anatase TiO_2 are observed in both patterns, such as peak (101) at $2\theta = 25.0°$ and peak (200) at $2\theta = 47.9°$. Diffraction peaks of Ti substrate are also found in these patterns, as evidenced by its typical peak (101) at $2\theta = 40.0°$. It has been discovered that the as-deposited MoO_3 on TiO_2 nanotubes is amorphous [36], but transforms to α phase with post heat treatment, as evidenced by its diffraction peaks of (020), (040) and (060) at $2\theta = 12.6°$, 25.4° and 38.6°, respectively. The phase structure of MoO_3-deposited TiO_2 nanotubes is further confirmed by Raman spectroscopy (Fig. 3(b)). Anatase TiO_2 displays six Raman active modes at different wavenumbers in this spectrum; namely, E_g (144 cm^{-1}, 197 cm^{-1}, 638 cm^{-1}), A_{1g} (513 cm^{-1}), and B_{1g} (399 cm^{-1}, 519 cm^{-1}) [37]. The band positions at 289 cm^{-1}, 337 cm^{-1}, 666 cm^{-1}, 819 cm^{-1} and 995 cm^{-1} are assigned to the mode (B_{2g}, B_{3g}), (B_{1g}, A_g), (B_{2g}, B_{3g}), (A_g, B_{1g}) and (A_g, B_{1g}) of pure α-MoO_3, respectively [36], which is in good agreement with our XRD results.

The Li-ion intercalation behaviors of all bare and MoO_3-deposited TiO_2 nanotube arrays are compared to study the effect of MoO_3 on their electrochemical properties. Fig. 4(a) displays cycling performances of bare and deposited TiO_2 nanotubes over 50 electrochemical cycles at a current density of 50 $\mu A\ cm^{-2}$ with two initial cycles at a small current of 10 $\mu A\ cm^{-2}$ within a potential range from 0.05 V to 3.0 V versus Li/Li^+. Obviously, a rapid capacity drop occurs at the first two cycles for all samples, mainly due to
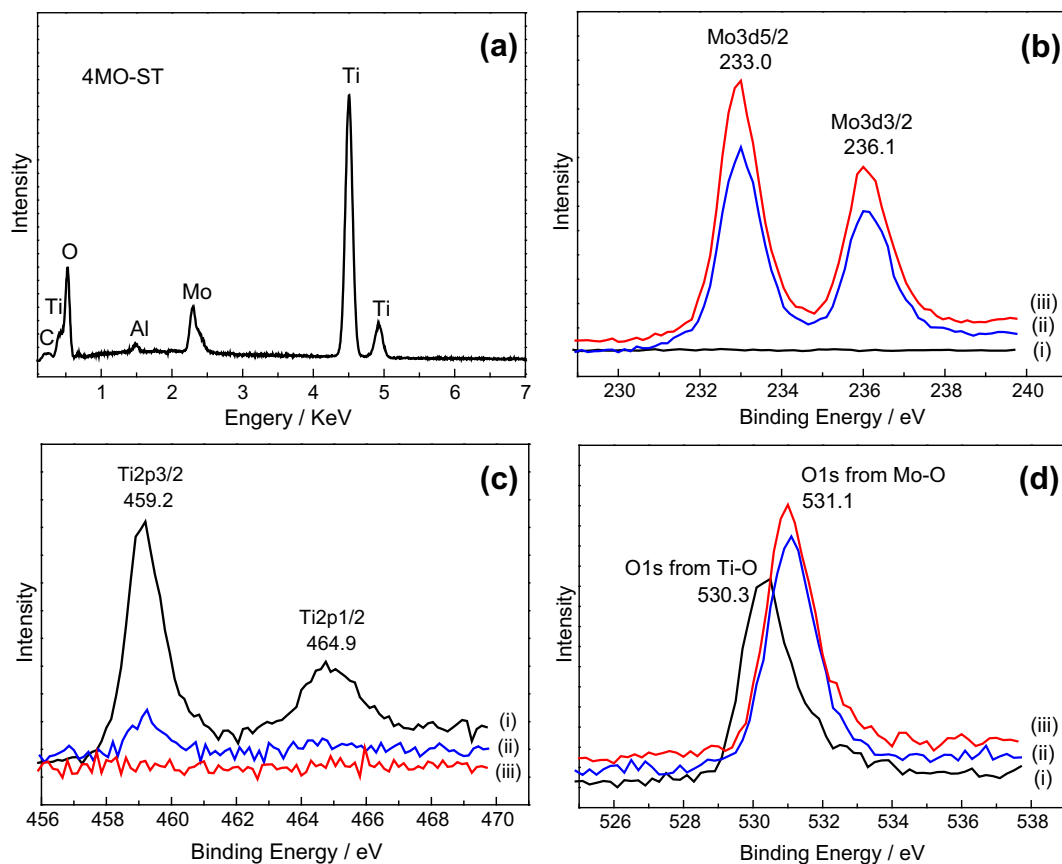
Fig. 2. (a) EDS spectrum of 4MO-ST, high-resolution XPS spectra of (b) Mo3d, (c) Ti2p and (d) O1s signals taken from (curve i) B-ST, (curve ii) 1MO-ST, and (curve iii) 4MO-ST.

decomposition of electrolyte and formation of SEI films on the surface of TiO_2 anodes. Their capacities decrease again upon the current switched to 50 $\mu A\ cm^{-2}$ at the third cycle, but soon stop fast decay and tend to stabilize. It is interestingly found that all MoO_3-deposited TiO_2 anodes deliver significantly higher capacities than the bare one. For example, 4MO-ST delivers the largest discharge capacity of 204.7 $\mu Ah\ cm^{-2}$ and charge capacity of 189.8 $\mu Ah\ cm^{-2}$ at the third cycle, more than two times of discharge (81.2 $\mu Ah\ cm^{-2}$) and charge (69.2 $\mu Ah\ cm^{-2}$) capacities of B-ST. Particularly, 1MO-ST with only one electrodeposition cycle of MoO_3 enables the capacity of TiO_2 anode to be nearly doubled, and the

capacity of MoO_3-coated TiO_2 nanotubes goes up as the deposition cycle increases from one to four, since 1MO-ST and 2MO-ST deliver discharge capacities of 154.9 $\mu Ah\ cm^{-2}$ and 183.1 $\mu Ah\ cm^{-2}$ at the third cycle. However, 6MO-ST exhibits a smaller capacity of 189.6 $\mu Ah\ cm^{-2}$ with respect to 4MO-ST, indicating that superfluous MoO_3 precipitates on nanotubes fail to further improve capacities of the composite anode. Specific capacities of these bare and MoO_3-coated TiO_2 nanotubes are obtained as well (Fig. S2). Similarly, 4MO-ST shows the highest capacities of 277.6–227.9 $mAh\ g^{-1}$ at 50 $\mu A\ cm^{-2}$ over 48 cycles, while B-ST displays the lowest capacities of 131–97.6 $mAh\ g^{-1}$ in the same conditions. The
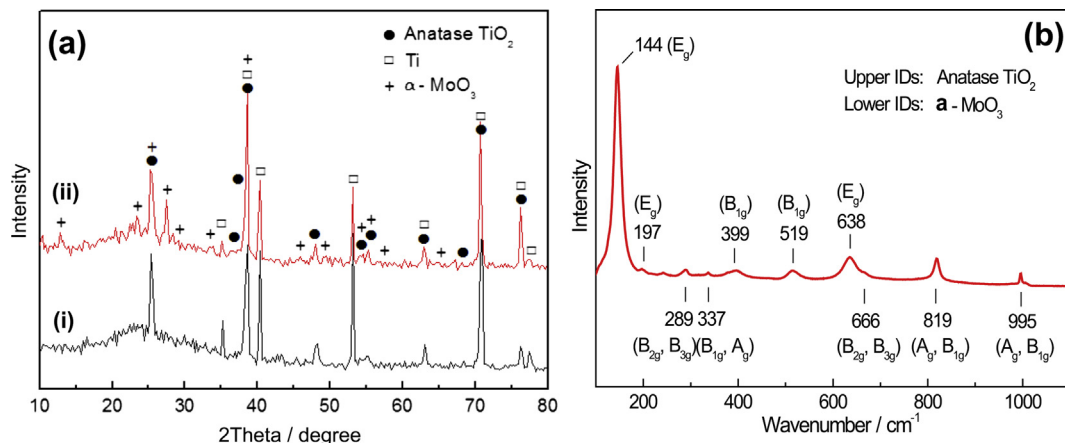
Fig. 3. (a) X-ray diffraction patterns of (curve i) B-ST and (curve ii) 4MO-ST, (b) Raman spectrum of 4MO-ST.
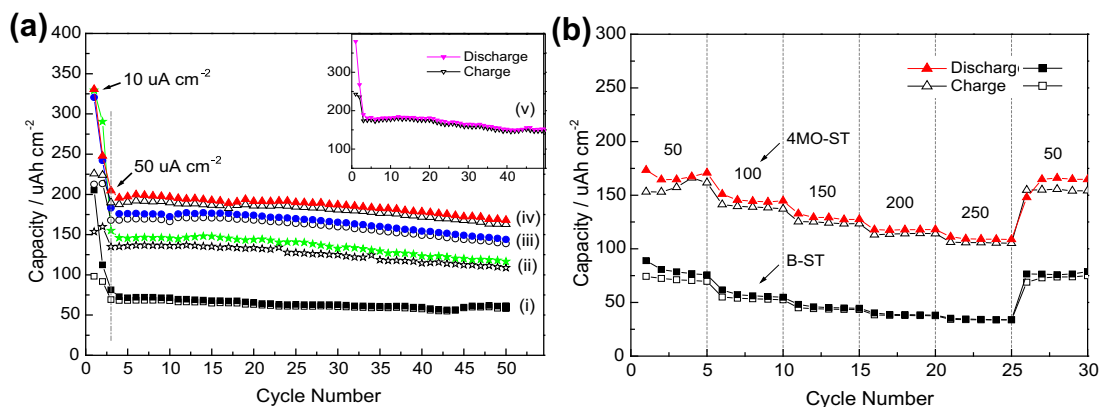
Fig. 4. (a) Areal discharge (solid symbol) and charge (hollow symbol) capacities of (curve i) B-ST, (curve ii) 1MO-ST, (curve iii) 2MO-ST, (curve iv) 4MO-ST and (curve v) 6MO-ST over 50 cycles measured at a current of 50 μA cm^{-2} with two initial cycles at 10 μA cm^{-2}; (b) Rate capability of B-ST and 4MO-ST at different current from 50 to 250 μA cm^{-2} after two initial cycles at 10 μA cm^{-2}.

porous MoO$_3$/TiO$_2$ nanotube composite structure can even possess larger Li-ion insertion capacities than dense MoO$_3$ powder electrodes which show a capacity of ~125 mAh g^{-1} with similar current and potential parameters for battery cycling, mostly due to faster Li-ion diffusion in porous electrodes [38]. In addition to capacity increment, the cycleability of TiO$_2$ anode is enhanced by MoO$_3$, as evidenced by capacity retention efficiency over the last 48 battery cycles of 75.3%–82.1% for the deposited samples, but only of 73.4% for the bare one. Moreover, MoO$_3$ could improve rate performance of TiO$_2$ nanotubes as well. Fig. 4(b) shows the capacity of 4MO-ST is more than twice that of B-ST at cycling current from 50 μA cm^{-2} ramped to 250 μA cm^{-2}. In conclusion, these results demonstrate that the combination of α-phase MoO$_3$ which has a large specific capacity to anatase TiO$_2$ nanotubes is able to not only boost their charge−discharge capacities, but also endow them with remarkable rate capability. Meanwhile, the TiO$_2$ tubular structure also plays an important role in the Li-ion insertion property of such composite electrodes. It allows efficient MoO$_3$ deposition onto its larger surface and sustains MoO$_3$ particles with volume change, transporting electrons and contributing to the overall capacity. Therefore, the MoO$_3$ coating makes self-standing TiO$_2$ nanotubes a very promising candidate for anode materials in compact LIBs with excellent performance. On the other hand, an overly thick and dense MoO$_3$ layer grown onto TiO$_2$ nanotube arrays is unfavorable for their electrochemical behaviors. It reduces porosity and contact area between electrode and electrolyte, and hinders Li-ion transfer to reach in-depth part of the oxide layer to utilize TiO$_2$ or MoO$_3$ there, yielding lower capacities of 6MO-ST compared to 4MO-ST. Actually, the advantages of a porous structure over a dense one have been extensively reported in literature about both TiO$_2$ and MoO$_3$, because Li-ion diffusion kinetics is truly facilitated in porous TiO$_2$ or MoO$_3$ films [18,38]. Since the porosity of TiO$_2$ nanotube anodes is reduced by MoO$_3$ deposition, the resulting negative effect on their Li-ion insertion performance can be compensated to some extent by the large specific capacity of α-MoO$_3$. Therefore, the capacity of deposited TiO$_2$ anodes continues to arise until six MoO$_3$ deposition cycles, in which circumstance a too thick and dense MoO$_3$ layer fully covers TiO$_2$ nanotubes and badly slows down Li-ion transfer.

Fig. 5(a) shows the galvanostatic discharge−charge curves of B-ST, 4MO-ST and 6MO-ST on the first and final cycle at a current of 50 μA cm^{-2} after two initial cycles at 10 μA cm^{-2}. It is clearly seen that these charge−discharge capacities of both deposited samples are more than twice those of the bare one. Two voltage plateaus appear near 1.7 V and 2.0 V in the curves of the three samples. The one at 1.70 V during discharging probably corresponds to Li-ion

insertion into anatase TiO$_2$ matrix, while the other in the charge plot accords with Li-ion desertion from TiO$_2$. The total chemical reaction for Li-ion insertion to/extraction from TiO$_2$ is described by Ref. [15]:

$$TiO_2 + xLi^+ + xe^- \leftrightarrow Li_xTiO_2 \tag{1}$$

For anatase TiO$_2$, x could be up to 0.5, corresponding to a capacity of 168 mAh g^{-1}. It has a tetragonal structure (space group I41/amd) in which a Ti^{4+} ion is surrounded by a distorted oxygen octahedron while numerous vacant octahedral and tetrahedral sites exist between these octahedrons. Li$^+$ ions can be accommodated in these vacant sites [15].

As the cell is discharged below 1.0 V, the capacity of B-ST continues to arise somewhat as shown by a decline slope of its plot in Fig. 5(a). Besides a little extra Li-ion insertion to TiO$_2$, an important reason for the increment could be the decomposition of electrolyte components at the TiO$_2$ electrodes in which Li$^+$ ions may participate to cause a few irreversible capacities [39,40]. In addition, more prolonged, slowly declined slopes below 0.7 V in discharge plots are observed for 4MO-ST and 6MO-ST, suggesting a remarkable amount of Li$^+$ ions intercalated into MoO$_3$-deposited TiO$_2$ nanotubes rather than bare ones at low potentials. Such difference is again confirmed by their differential capacity curves derived from this figure. Fig. 5(b) shows a pair of oxidation peak (at 2.06 V) and reduction peak (at 1.70 V) during the charge−discharge process of anatase TiO$_2$, together with two extra small peaks (at 2.11 V and 1.43 V) on the side, suggesting a one-stage lithiation mechanism in anatase TiO$_2$ according to Eq. (1). When the potential drops to 0.05 V, a few excessive Li$^+$ ions are inserted into TiO$_2$ or reacted with electrolytes. It is also found that after 48 electrochemical cycles, the reduction and oxidation peaks for B-ST are weakened, due to fewer sites in TiO$_2$ matrix for Li-ion intercalation. However, the peak positions almost remain unchanged, which claims good reversibility of Li-ion insertion/desertion reaction on TiO$_2$. On the contrary, the lithiation process in MoO$_3$-deposited samples appears greatly different. Fig. 5(c) displays the differential capacity curve of 4MO-ST. In this figure, the strong peaks at 1.71 V and 2.05 V mainly correspond to Li-ion insertion and desertion on TiO$_2$. Nevertheless, the peak at 1.57 V and multiple peaks over 0.08–0.45 V in the discharge plot are assigned to Li-ion intercalation into MoO$_3$, and the oxidation peaks at 2.1 V and 2.21 V are related to extraction of Li$^+$ ions from MoO$_3$. In addition, there is a broad, low plateau between 1.2 V and 2 V in the charge plot, suggesting the release of a small number of Li$^+$ ions from MoO$_3$ within this potential window, which is according to the linearly increasing slope of 4MO-ST in Fig. 5(a). Actually, the peaks are attributed to a two-stage lithiation
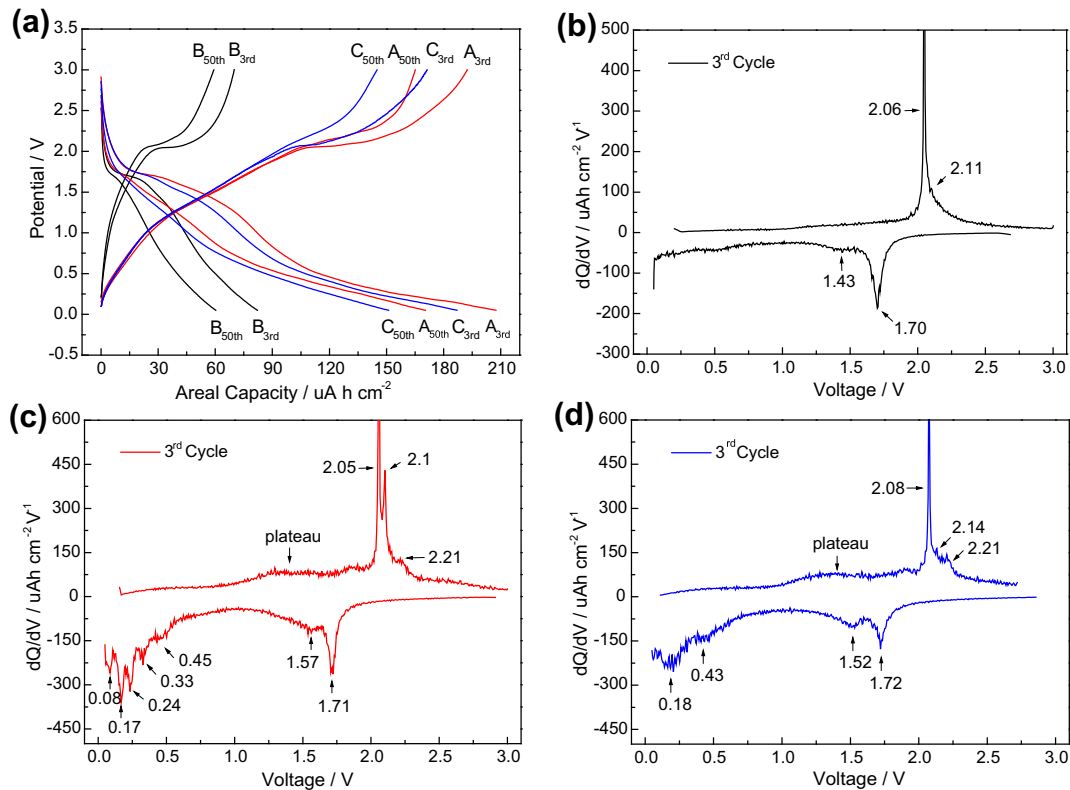
Fig. 5. (a) Charge–discharge profiles at the 3rd and 50th cycle of B-ST (B$_{3rd}$, B$_{50th}$), 4MO-ST (A$_{3rd}$, A$_{50th}$) and 6MO-ST (C$_{3rd}$, C$_{50th}$), and their according differential capacity curves of (b) B-ST, (c) 4MO-ST and (d) 6MO-ST measured at a current of 50 μA cm^{-2} after two initial cycles at 10 μA cm^{-2}.

process in α-MoO$_3$ [34,38]. As the potential is above 1.25 V, the reaction of Li-ion insertion into MoO$_3$ on TiO$_2$ anode can be described by Ref. [34]:

$$MoO_3 + xLi^+ + xe^- \leftrightarrow Li_xMoO_3 \tag{2}$$
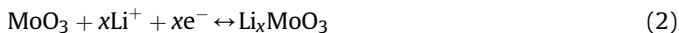
For α-MoO$_3$, x could be between 1 and 1.5 in the first stage. The α-MoO$_3$ has an orthorhombic structure containing distorted MoO$_6$ octahedra. They share edges and form chains that are cross-linked through oxygen atoms to yield layers. Li$^+$ ions are accommodated in the interlayer spacing between these octahedral layers and intralayers [41]. Most of them would move out of MoO$_3$ matrix in the charging process, leading to excellent reversibility of the reaction shown in Eq. (2).

Fig. 6. EIS and equivalent circuit of half cells containing B-ST, 2MO-ST, 4MO-ST and 6MO-ST anodes measured at a potential of 1.7 V after electrochemical cycles.

The second stage of Li-ion intercalation into MoO$_3$ occurs at potentials below 0.7 V here, and the according reaction can be expressed by Ref. [34]:

$$Li_xMoO_3 + yLi^+ + ye^- \leftrightarrow Mo + 3Li_2O \tag{3}$$

It can be seen from Eq. (3) that in lower voltage regions Li$^+$ ions react with the solid solution (Li$_x$MoO$_3$) to form Mo metal and Li$_2$O oxides. Li$_2$O is believed to be naturally irreversible, but the presence of nanosized Mo particles induces a reversible reaction of Li$_2$O during charging [34,38], and thus a huge loss of active material is prohibited. As a result, the reversibility of formed Li$_2$O ensures all the MoO$_3$-deposited TiO$_2$ nanotubes to deliver comparable columbic efficiencies (>90%) and capacity retention efficiencies to the bare ones as shown in Fig. 4(a). Similar reduction and oxidation peaks are found almost in the same positions on the differential capacity curves of 1MO-ST and 2MO-ST but with lower height, suggesting that more Li$^+$ ions involve into the insertion/desertion reactions at 4MO-ST. As for 6MO-ST, it gives a similar differential capacity plot as well, but the height of its peaks is relatively lower than that of peaks for 4MO-ST (Fig. 5(d)). In brief, these electrochemical characteristics vividly account for the distinct differences in the Li-ion intercalation capacity and cycling performance of both MoO$_3$-deposited and bare TiO$_2$ nanotube anodes. However, after 48 electrochemical cycles, all the peaks shown in Fig. 5(b)–(d) weaken or even disappear, indicating that a slow capacity loss is also inevitable for MoO$_3$-deposited TiO$_2$ anodes in prolonged cycles. One reason for this event could be the electrolyte decomposition as batteries are cycled within low potential regions [39].

As discussed above, the MoO$_3$ precipitates reduce the porosity of TiO$_2$ nanotube arrays and probably hinder Li-ion transfer inside the composite anodes. In order to verify this assumption, electrochemical impendence spectroscopy (EIS) technique is employed to study Li-ion transfer kinetics on the bare and MoO$_3$-deposited TiO$_2$
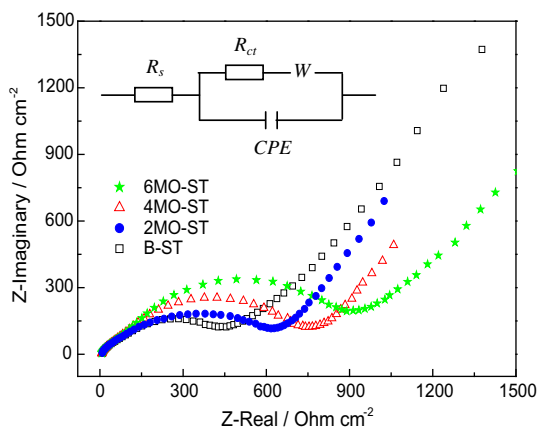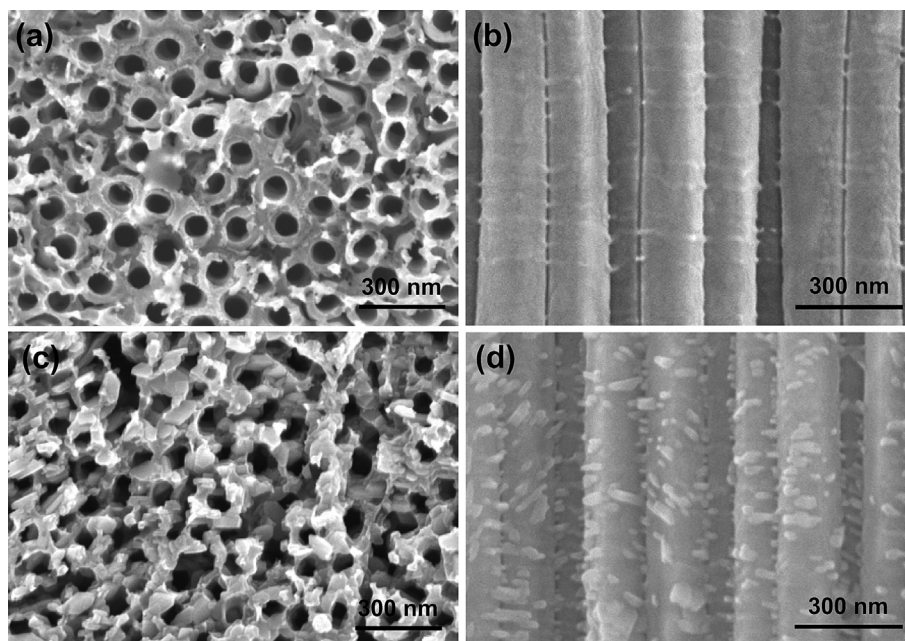
Fig. 7. SEM images of (a, b) B-LT, (c, d) 4MO-LT films synthesized by anodic oxidation of Ti in EG + 0.3 wt% NH_4F + 5 vol% H_2O at 70 V for 40 min, and subsequent electrodeposition of MoO_3 for 0 and 4 cycles, respectively.

anodes. Fig. 6 shows Nyquist plots and their equivalent circuit for B-ST, 2MO-ST, 4MO-ST and 6MO-ST after cells were discharged and charged for nine cycles. In this circuit, R_s is the ohmic resistance from the electrolyte, separator and electrodes, corresponding to the intercept of depressed semicircle in high-to-medium frequency region with the Z-Real axis. This semicircle is related to the Li-ion transfer process from electrolyte into TiO_2 anode. R_{ct} is the charge transfer resistance, which can be inferred from the semicircle arc. The sloping line at low frequency range represents Li-ion diffusion in the bulk electrode, known as the Warburg impedance (W). From these plots, it is found that the semicircle diameter for 2MO-ST is longer than that for B-ST, implying larger charge transfer resistance (R_{ct}) in the former than in the latter. Moreover, R_{ct} is further increased for 4MO-ST and 6MO-ST with more MoO_3 deposition cycles. The EIS analyses reveal that Li-ion transfer at TiO_2 anode is indeed hindered by MoO_3 coating. When the MoO_3 layer is thickened, Li-ion transfer becomes more difficult in the composite anodes. However, MoO_3 with the nature of large specific capacity accepts more Li^+ ions to achieve capacity increment on 2MO-ST and

4MO-ST. As the MoO_3 coating tends to be too thick and dense on 6MO-ST, Li-ion diffusion is greatly retarded and fewer Li^+ ions could be effectively accommodated into MoO_3 and TiO_2 crystals, yielding reduced Li-ion insertion capacities in comparison with 4MO-ST.

As we discussed before, the porosity of thin film anodes has a significant impact on their Li-ion intercalation performance, and thereby we optimize the structure of anodic TiO_2 nanotubes to further increase the capacity of MoO_3-deposited TiO_2 anodes. Dimensions of TiO_2 nanotubes could be easily and precisely tuned by changing parameters (voltage, electrolyte composition and time) for anodic oxidation of Ti [17]. Fig. 7(a) and (b) presents SEM images of larger TiO_2 nanotubes (B-LT) synthesized by anodizing Ti in EG + 0.3 wt% NH_4F + 5 vol% H_2O electrolytes at 70 V for 40 min. The top-view SEM image in Fig. 7(a) shows considerable well-ordered TiO_2 nanotubes with an inner diameter of 80 nm and a wall thickness of 42 nm. They possess a larger outer diameter of ∼168 nm (Fig. 7(b)) and longer length of ∼9.0 μm (Fig. S3a) than the above TiO_2 nanotubes (B-ST) fabricated at lower voltage (60 V) and short time (30 min) in water-rich electrolytes (10 vol%). In addition, outer
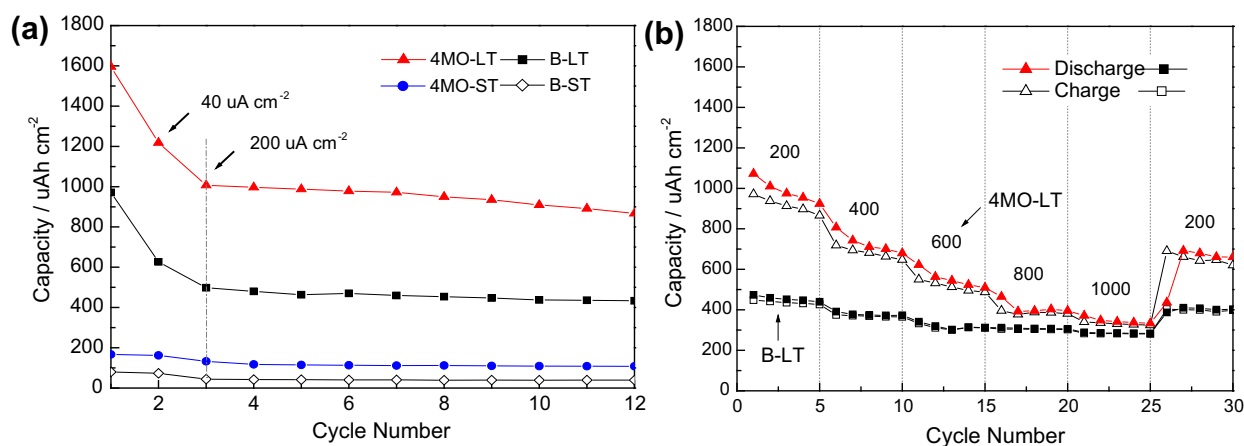
Fig. 8. (a) Areal discharge capacities over 12 cycles of bare and MoO_3-deposited TiO_2 nanotubes measured at a current of 200 μA cm^{-2} with two initial cycles at 40 μA cm^{-2}; (b) Rate capability of B-LT and 4MO-LT at different current from 200 to 1000 μA cm^{-2} after two initial cycles at 40 μA cm^{-2}.

walls of B-LT are relatively smooth, only with a few tiny ridges on the surface that connect neighboring tubes. Later, they are deposited with MoO$_3$ via 4 deposition cycle (4MO-LT). With post-heat treatment, the walls of deposited nanotubes become thicker and their inner diameter is reduced to ~52 nm due to formation of MoO$_3$ (Fig. 7(c)). The MoO$_3$ nanoparticles are grown not only on the top of TiO$_2$ nanotubes, but also on their tube walls. It can be seen in Fig. 7(d) that numerous particles anchored on the outer walls of TiO$_2$ nanotubes, with a broad size range of up to 90 nm. They are uniformly present from the tube entrance to tube bottom, as observed from SEM image of rough tube walls (Fig. S3b) and an EDS mapping image of Mo element taken from the cross-sectional view (Fig. S4a). An EDS analysis also reveals the existence of both TiO$_2$ and MoO$_3$ (~14.3 wt %) on 4MO-LT (Fig. S4b). Apparently, the porous structure is preserved well after MoO$_3$ deposition, and the hollow tubes not only serve as a support for MoO$_3$, but also provide numerous channels to let electrolyte easily infiltrate and Li$^+$ ions quickly transfer, and therefore better Li-ion insertion properties of such MoO$_3$-deposited TiO$_2$ nanotube anodes are anticipated.

Fig. 8(a) exhibits cycling performances of bare (B-ST, B-LT) and deposited TiO$_2$ nanotubes (4MO-ST, 4MO-LT) over 12 electrochemical cycles at a current of 200 μA cm^{-2} with two initial cycles at a small current of 40 μA cm^{-2} in a potential range from 0.05 V to 3.0 V versus Li/Li$^+$. Interestingly, both large TiO$_2$ nanotubes display higher capacities than the two small nanotubes. For example, B-LT delivers a charge capacity almost nine times that of B-ST over 10 cycles at 200 μA cm^{-2}, owing to its more active mass and larger surface area. Likewise, 4MO-LT also exhibits capacities between 867.2 μAh cm^{-2} and 1007.2 μAh cm^{-2}, eight times as high as those (107.9–132.9 μAh cm^{-2}) of 4MO-ST, which is ascribed to much more TiO$_2$ and MoO$_3$ involved in Li-ion intercalation process. Again, the capacity of B-LT is doubled by MoO$_3$ deposition of 4 cycles (4MO-LT). It is worth noting that such high areal capacities of modified anodic TiO$_2$ nanotubes are firstly achieved with respect to the nanotubes coated with metals or other oxides that only deliver capacities of 100–680 μAh cm^{-2} at smaller current of 20–100 μA cm^{-2} within similar potential ranges [24–33]. In addition, the specific capacities up to ~387.4 mAh g^{-1} for 4MO-LT make it comparable to composites of anodic TiO$_2$ nanotubes with Fe$_2$O$_3$ [32], Co$_3$O$_4$ and NiO [30], and even carbon materials. Moreover, 4MO-LT shows better rate capability than B-LT when the current increases from 200 to 1000 μA cm^{-2} (Fig. 8(b)), which agrees well with the enhanced rate capability of 4MO-ST above. These results indicate that increasing the pore size and especially the tube length for MoO$_3$-deposited TiO$_2$ nanotubes is an effective way to enhance the Li-ion intercalation properties of TiO$_2$ thin film anodes.

4. Conclusions

In summary, anatase TiO$_2$ nanotube arrays have been synthesized by anodic oxidation of Ti in NH$_4$F-containing EG electrolyte and post-heat treatment. These nanotubes are then modified by electrodeposition of MoO$_3$ for various cycles. Alpha-phase MoO$_3$ particles are anchored on the nanotubes to significantly improve both the Li-ion insertion capacities and cycleability of TiO$_2$ anode in lithium-ion batteries. Such improvement could be further optimized either by tuning the number of deposition cycles, or by increasing the dimension of anodic TiO$_2$ nanotubes. The excellent Li-ion intercalation behavior of MoO$_3$/TiO$_2$ composite anode is mainly attributed to MoO$_3$ with the nature of a high specific capacity and TiO$_2$ porous structure with large surface area for ionic transfer. Our results indicate that nanosized TiO$_2$ anodes composited with other materials having large specific Li-ion insertion capacities could be a promising material for the anode of high-performance LIBs.

Appendix A. Supplementary data

Supplementary data related to this article can be found at http://dx.doi.org/10.1016/j.jpowsour.2013.07.096.

References

[1] J.M. Tarascon, M. Armand, Nature 414 (2001) 359–367.
[2] A.S. Arico, P. Bruce, B. Scrosati, J.M. Tarascon, W. Van Schalkwijk, Nat. Mater. 4 (2005) 366–377.
[3] A.R. Armstrong, G. Armstrong, J. Canales, P.G. Bruce, J. Power Sources 146 (2005) 501–506.
[4] M. Winter, J.O. Besenhard, M.E. Spahr, P. Novak, Adv. Mater. 10 (1998) 725–763.
[5] I. Rom, M. Wachtler, I. Papst, M. Schmied, J.O. Besenhard, F. Hofer, M. Winter, Solid State Ionics 143 (1999) 329–336.
[6] S.K. Sharma, M.-S. Kim, D.Y. Kim, J.-S. Yu, Electrochim. Acta 87 (2013) 872–879.
[7] W.J. Zhang, J. Power Sources 196 (2011) 13–24.
[8] T. Tao, A.M. Glushenkov, C.F. Zhang, H.Z. Zhang, D. Zhou, Z.P. Guo, H.K. Liu, Q.Y. Chen, H.P. Hu, Y. Chen, J. Mater. Chem. 21 (2011) 9350–9355.
[9] N. Du, H. Zhang, B.D. Chen, J.B. Wu, X.Y. Ma, Z.H. Liu, Y.Q. Zhang, D.R. Yang, X.H. Huang, J.P. Tu, Adv. Mater. 19 (2007) 4505–4509.
[10] W.-S. Kim, Y. Hwa, J.-H. Jeun, H.-J. Sohn, S.-H. Hong, J. Power Sources 225 (2013) 108–112.
[11] W.J. Li, Z.W. Fu, Appl. Surf. Sci. 256 (2010) 2447–2452.
[12] W.-S. Chang, C.-M. Park, J.-H. Kim, Y.-U. Kim, G. Jeong, H.-J. Sohn, Energy Environ. Sci. 5 (2012) 6895–6899.
[13] S.Y. Yin, L. Song, X.Y. Wang, M.F. Zhang, K.L. Zhang, Y.X. Zhang, Electrochim. Acta 54 (2009) 5629–5633.
[14] M. Fehse, F. Fischer, C. Tessier, L. Stievano, L. Monconduit, J. Power Sources 231 (2013) 23–28.
[15] D.S. Guan, C. Cai, Y. Wang, J. Nanosci. Nanotechnol. 11 (2011) 3641–3650.
[16] D. Deng, M.G. Kim, J.Y. Lee, J. Cho, Energy Environ. Sci. 2 (2009) 818–837.
[17] D. Guan, P.J. Hymel, Y. Wang, Electrochim. Acta 83 (2012) 420–429.
[18] G.F. Ortiz, I. Hanzu, T. Djenizian, P. Lavela, J.L. Tirado, P. Knauth, Chem. Mater. 21 (2009) 63–67.
[19] X. Su, Q.L. Wu, X. Zhan, J. Wu, S.Y. Wei, Z.H. Guo, J. Mater. Sci. 47 (2012) 2519–2534.
[20] H.T. Fang, M. Liu, L.W. Wang, T. Sun, D.S. Guan, F. Li, J.G. Zhou, T.K. Sham, H.M. Cheng, Nanotechnology 20 (2009) 225701.
[21] N.A. Kyeremateng, F. Vacandio, M.-T. Sougrati, H. Martinez, J.-C. Jumas, P. Knauth, T. Djenizian, J. Power Sources 224 (2013) 269–277.
[22] D.W. Liu, Y.H. Zhang, P. Xiao, B.B. Garcia, Q.F. Zhang, X.Y. Zhou, Y.-H. Jeong, G.Z. Cao, Electrochim. Acta 54 (2009) 6816–6820.
[23] D.W. Liu, P. Xiao, Y.H. Zhang, B.B. Garcia, Q.F. Zhang, Q. Guo, R. Champion, G.Z. Cao, J. Phys. Chem. C 112 (2008) 11175–11180.
[24] H.S. Kim, S.H. Kang, Y.H. Chung, Y.-E. Sung, Electrochem. Solid-State Lett. 13 (2010) A15–A18.
[25] Y.H. Zhang, Y.N. Yang, P. Xiao, X.N. Zhang, L. Lu, Lu Li, Mater. Lett. 63 (2009) 2429–2431.
[26] D.S. Guan, Y. Wang, Ionics 19 (2013) 879–885.
[27] X.Q. Meng, J.Y. Yao, F.L. Liu, H.C. He, M. Zhou, P. Xiao, Y.H. Zhang, J. Alloys Compd. 552 (2013) 392–397.
[28] L.L. Wang, S.C. Zhang, X.M. Wu, Chem. Lett. 40 (2011) 1428–1430.
[29] Y.Q. Fan, N. Zhang, L.Y. Zhang, H.B. Shao, J.M. Wang, J.Q. Zhang, C.N. Cao, Electrochim. Acta 94 (2013) 285–293.
[30] N.A. Kyeremateng, C. Lebouin, P. Knauth, T. Djeniziana, Electrochim. Acta 88 (2013) 814–820.
[31] M. Yang, G. Yang, E. Spiecker, K. Lee, P. Schmuki, Chem. Commun. 49 (2013) 460–462.
[32] L. Yu, Z.Y. Wang, L. Zhang, H.B. Wu, X.W. Lou, J. Mater. Chem. A 1 (2013) 122–127.
[33] L.G. Xue, Z. Wei, R.S. Li, J.L. Liu, T. Huang, A.S. Yu, J. Mater. Chem. 21 (2011) 3216–3220.
[34] P. Meduri, E. Clark, J.H. Kim, E. Dayalan, G.U. Sumanasekera, M.K. Sunkara, Nano Lett. 12 (2012) 1784–1788.
[35] K. Lorenz, S. Bauer, K. Gutbrod, J.P. Guggenbichler, P. Schmuki, C. Zollfrank, Biointerphases 6 (2011) 16–21.
[36] D. Yao, J.Z. Ou, K. Latham, S. Zhuiykov, A.P. O'Mullane, K. Kalantar-Zadeh, Cryst. Growth Des. 12 (2012) 1865–1870.
[37] H.C. Choi, Y.M. Jung, S.B. Kim, Vib. Spectrosc. 37 (2005) 33–38.
[38] G.Y. Zhao, N.Q. Zhang, K.N. Sun, J. Mater. Chem. A 1 (2013) 221–224.
[39] S.-K. Jeong, M. Inaba, T. Abe, Z. Ogumi, J. Electrochem. Soc. 148 (2001) A989–A993.
[40] K. Tasaki, A. Goldberg, J.J. Lian, M. Walker, A. Timmons, S.J. Harrisc, J. Electrochem. Soc. 156 (2009) A1019–A1027.
[41] B.C. Windom, W.G. Sawyer, D.W. Hahn, Tribol. Lett. 42 (2011) 301–310.